Single-cell identification with quantum-enhanced nuclear magnetic resonance

Zhiyuan Zhao[1,2†], Qian Shi[1,2†], Shaoyi Xu[1], Xiangyu Ye[1], Mengze Shen[1], Jia Su[1], Ya Wang[1,2,3], Tianyu Xie[1,2], Qingsong Hu[5], Fazhan Shi[1,2,3,4,5*], Jiangfeng Du[3,6*]

[1]Laboratory of Spin Magnetic Resonance, School of Physical Sciences,
Anhui Province Key Laboratory of Scientific Instrument Development and Application,
University of Science and Technology of China, Hefei 230026, China
[2]Hefei National Research Center for Physical Sciences at the Microscale,
University of Science and Technology of China, Hefei 230026, China
[3]Hefei National Laboratory, University of Science and Technology of China, Hefei 230088, China
[4]School of Biomedical Engineering and Suzhou Institute for Advanced Research,
University of Science and Technology of China, Suzhou 215123, China
[5]The First Affiliated Hospital of USTC, Division of Life Sciences and Medicine,
University of Science and Technology of China, Hefei 230026, China
[6]State Key Laboratory of Ocean Sensing and School of Physics,
Zhejiang University, Hangzhou 310058, China

[†]These authors contributed equally to this work.
[*]E-mail: fzshi@ustc.edu.cn; djf@ustc.edu.cn

Identification of individual cells within heterogeneous populations is essential for biomedical research and clinical diagnostics. Conventional labeling-based sorting methods, such as fluorescence-activated cell sorting and magnetic-activated cell sorting, enable precise sorting when reliable markers are available. However, their applicability is limited in cells lacking defined markers or sensitive to labeling, as labeling can compromise cellular viability and function. We

present a single-cell identification approach using quantum-enhanced NMR with diamond nitrogen-vacancy centers for label-free detection of intracellular proton (^{1}H) signals. Using this method, we distinguish two human tumor cell lines by their proton spin-lattice (T_1) relaxation times, which serve as a cell-intrinsic physicochemical signature. It lays the groundwork for label-free sorting applications in rare cell analysis, personalized medicine, and single-cell diagnostics.

Introduction

Cells represent fundamental units of biological research, providing insights into physiological functions, disease mechanisms, and therapeutic strategies (*1–4*). Extracting meaningful information from heterogeneous cell populations often requires identifying and isolating specific cell types. (*5–7*). Conventional techniques, including fluorescence-activated cell sorting (FACS) (*8, 9*) and single-cell sequencing technologies (*10*), have significantly advanced single-cell studies. However, while FACS depends on known cell-surface markers and often requires antibody-based fluorescent labeling, single-cell sequencing approaches, though not necessarily label-dependent, still rely on pre-isolated cell populations and cannot preserve native cellular states (*11*). Consequently, cells lacking distinctive markers or those whose physiological conditions may be perturbed during processing remain challenging to identify and isolate accurately (*12*). These limitations underscore the need for developing label-free, live-cell single-cell characterization technologies.

Nuclear magnetic resonance (NMR), a technique that detects various nuclear spins in biological samples, offers label-free, non-destructive access to molecular composition and dynamics in living cells (*13–15*). These features have underpinned its widespread use in structural biology and clinical diagnosis. However, conventional NMR lacks the spatial resolution re-

quired for single-cell analysis. Most measurements rely on ensemble averaging across large populations, obscuring cellular heterogeneity (*16–18*). Cell-resolved measurements have been demonstrated only for giant cells at the nL scale ($\sim$100 μm), whereas typical mammalian somatic cells at the pL scale ($\sim$10 μm) remain beyond reach (*19*).

Recent advancements in quantum technologies, particularly nitrogen-vacancy (NV) centers in diamond, have transformed magnetic sensing by dramatically improving both sensitivity and spatial resolution (*20–23*). NV-based quantum sensors enable nanoscale detection (*24–28*) and chemical resolved spectra (*29–31*), offering an unparalleled platform for cellular-scale analysis. Despite this progress, the application of such technologies to single-cell analysis has remained elusive. Here, we demonstrate NV-based single-cell NMR, enabling a label-free strategy for cell identification (Fig. 1). We validate the strategy in HeLa and MCF7 cells by measuring proton spin-lattice T_1 relaxation as the first example. This approach links intrinsic physicochemical signatures to cell identity and opens new opportunities in fundamental biological research and clinical diagnostics, including rare cell analysis (*32, 33*), personalized medicine (*34, 35*), and single-cell diagnostics (*36, 37*).

Principles of single-cell nuclear magnetic resonance

In biological systems, the dominant elements carbon, hydrogen, nitrogen and phosphorus (^{13}C, ^{1}H, ^{14}N, and ^{31}P) naturally possess nuclear spins. Among them, proton (^{1}H) is the most abundant nuclear spin, arising from intracellular water molecules and all biomolecules. Single-cell nuclear magnetic resonance (NMR) exploits the magnetic dipolar interaction between these nuclear spins and the electronic spin of a diamond NV sensor. Under an external magnetic field aligned with the NV axis, the NV sensor-target nuclear coupling Hamiltonian for a single

nucleus is given by

$$H = \underbrace{DS_z^2 + \gamma_e B_0 S_z}_{\text{Sensor}} + \underbrace{S_z \left(a_\parallel I_z + a_\perp I_\perp\right)}_{\text{Sensor-target coupling}} + \underbrace{\gamma_n B_0 I_z}_{\text{Target nuclear spin}} , \tag{1}$$

where D is the zero-field splitting, γ_e and γ_n are the electronic and nuclear gyromagnetic ratios, S_z denotes the NV electron spin operator, and I_z, $I_\perp$ are the spin components with longitudinal and transverse dipolar couplings $a_\parallel$ and $a_\perp$. Here $I_\perp = \cos\phi I_x + \sin\phi I_y$, where ϕ and θ denote the azimuthal and polar angles between the NV axis and the nuclear spin. Neglecting Fermi contact terms, the longitudinal dipolar coupling strength is given by

$$a_\parallel = \frac{\mu_0 \gamma_e \gamma_n \hbar}{4\pi r^3}(3\cos^2\theta - 1), \tag{2}$$

where r is the NV-nucleus distance (see Fig. 1d). The longitudinal coupling can be interpreted as an effective static magnetic field along the NV axis (*24*). For multiple nuclei, the total Hamiltonian is obtained by summing over all nuclear spins, as detailed in the Supplementary Information.

Experimental implementation of single-cell NMR

Single-cell NMR is implemented on diamond micropillars that host individual near-surface NV centres at their tips, thereby providing intrinsically localised sensing volumes and avoiding the spatial averaging inherent in NV ensembles. A thin PDMS layer applies mild mechanical pressure that gently flattens cells onto the pillar array, improving contact with the diamond surface while expanding the lateral footprint of individual cells. The relative positions of cells and pillars are registered by optical microscopy and verified by confocal NV fluorescence scans at different focal planes, confirming that the pillars selected for NMR detectiont are fully enveloped by a single cell (Fig. 2a–d). To quantify the spatial origin of the detected signal, we evaluate the NV-detected NMR signal as a function of the lateral integration radius around a

given pillar. The integrated signal saturates at a radius comparable to the projected cell size, indicating that the dominant contribution arises from nuclei within a single cell (Fig. 2e).

While the NV-proton coupling provides the physical basis for detection, practical realization of single-cell NMR demands strategies to overcome inherently weak signals. Accordingly, enhancing the signal-to-noise ratio (SNR) requires both improvement of magnetic sensitivity and amplification of the nuclear signal. To enhance sensitivity while preserving spatial resolution, we used single NV centers in isotopically purified ^{12}C diamond (*38*) which provides millisecond-scale coherence times, together with real-time feedback charge-state preparation (*39, 40*) and repetitive readout protocols (*41*) to improve initialization and readout fidelity. Overhauser dynamic nuclear polarization (DNP) (*42, 43*) increased nuclear spin polarization thereby amplifying the nuclear signal.

Analogous to an optical interferometer, we employ a spin-based quantum interferometer to detect the proton signal. The nuclear magnetic signal detection sequence (Fig. 3a) consists of three stages: initialization, phase accumulation, and readout. In the initialization stage, real-time feedback charge-state initialization is employed to simultaneously prepare both the charge and spin states of the NV center. The second stage employs an electron-nuclear double resonance (ENDOR) sequence: a $\pi_x/2$ pulse prepares the NV electron spin in the $(|0\rangle + |1\rangle)/2$ state, followed by two π pulses applied to the electron spin while subsequent radio-frequency π pulses are applied to the sample nuclei. In this way, low-frequency environmental noise is suppressed while the NV-nuclear spin coupling is preserved. To suppress phase accumulation induced by radio-frequency (RF) control, a two-π pulse echo sequence is employed. Finally, a $\pi_y/2$ pulse is applied to read out the polarization signal,

$$P_{\mathrm{pola}} \approx \frac{1}{2} + \frac{P \sum_i a_{\parallel,i} \tau}{4}, \tag{3}$$

where P is the nuclear spin polarization. Because the polarization generated by DNP is opposite

to the thermal equilibrium polarization, continuous measurements following DNP yield the spin-lattice relaxation curve of protons. To prevent depolarization induced by imperfect control, adiabatic RF pulses were applied, and the amplitude was precisely calibrated. Calibration was performed by measuring the RF-induced Bloch-Siegert shift of the NV energy levels. In the final readout stage, the electronic state is transferred to the nuclear spin, enabling repetitive readout of the NV spin state. Further details of the experimental sequence are provided in the Supplementary Information.

Sweeping the RF frequency in the sequence yields the nuclear magnetic resonance spectrum in Fig. 3b. To confirm the signal originates from protons, we performed field-dependent measurements. By tracking the resonance positions at three magnetic field strengths, we obtained a slope of 4.24(2) kHz/G, in excellent agreement with the proton gyromagnetic ratio of 4.26 kHz/G. This confirms that the detected nuclear magnetic signal arises from intracellular proton spins. The linewidth is narrower than the power-broadened width of a single RF pulse because correlations between repetitions allow off-resonant pulse errors to accumulate, narrowing the line.

Validation of cell identification by single-cell NMR

Early NMR studies revealed tissue-dependent differences in nuclear spin relaxation (*44*), providing the physical and diagnostic basis for magnetic resonance imaging (MRI). Building on similar principle, we present a label-free strategy for cell identification using single-cell NMR contrasts and validate it by discriminating cell types via proton spin-lattice (T_1) relaxation measured in individual cells.

MCF7 cells (*45*), derived from human breast adenocarcinoma, are widely used as a model in cancer biology, whereas HeLa cells (*46*), originating from cervical carcinoma, are among the most extensively studied human cell lines. These two cell types were selected for single-cell

T_1 measurements to assess whether relaxation times can distinguish them. Fig. 4a and b show representative single-cell proton spin-lattice decays from an MCF7 cell and a HeLa cell, respectively, illustrating their different relaxation rates. The average T_1 for protons in MCF7 cells was $76(6)$ ms, whereas HeLa cells exhibited a longer average T_1 of $109(7)$ ms (Fig. 4c). Single-cell T_1 relaxation distinguishes MCF7 and HeLa populations ($p = 0.0049$), with a large effect size ($\delta = 0.78$) and a median T_1 difference of 36.5 ms. The T_1 distributions differ significantly between the two cell populations, demonstrating that single-cell T_1 relaxation times can be used to discriminate between distinct cell types.

Conclusion and outlook

We demonstrate label-free cell identification with NV-enhanced single-cell NMR. Measuring intracellular proton spin-lattice relaxation enables reliable discrimination between cell types without exogenous labels, thereby eliminating the dependence on cell-surface markers. These results establish T_1 as an intrinsic physicochemical signature of the intracellular microenvironment and position single-cell NMR as a physics-based modality for label-free classification.

At the cellular level, the spin-lattice relaxation time of intracellular water provides an integrated measure of the physicochemical microenvironment. Variations in T_1 arise from the interplay of protein-water interfaces, hydration dynamics, paramagnetic radicals and the ionic milieu (*47–51*). Analysis of our single-cell NMR data demonstrates that the spin-lattice relaxation time can discriminate between different cell types. To enhance discriminative power across diverse cell types and in highly heterogeneous samples, a natural extension is to incorporate additional NMR dimensions which are sensitive to complementary physicochemical variables, such as spin-spin relaxation time (T_2), chemical shifts, nuclear magnetic relaxation dispersion (NMRD) (*52*), magnetization transfer (*53*). These multi-parametric NMR contrasts provide complementary sensitivity to susceptibility-induced dephasing, molecular composition,

and rotational dynamics (*54*).

Our array-based implementation affords detailed single-cell measurements, but in its current form it only permits buffer solution to flow across the pillars rather than transporting cells, resulting in limited throughput and constraining population-scale analyses of heterogeneity. This limitation is imposed by the present fluidic design rather than by the NV-based detection itself. Integrating single-cell NMR with more advanced microfluidic platforms (*55–57*) offers a promising route to truly high-throughput, massively parallel measurements and large-scale datasets, paving the way for a single-cell NMR atlas (Fig. 4d).

Single-cell NMR provides unique access to relaxation, spectroscopic, and spatial information from the cell interior. With single-NV implementations, it can approach subcellular resolution and integrate with single-cell sequencing, single-cell transcriptomics, single-cell proteomics and single-cell metabolomics for multimodal cellular characterization (*10*). Such an approach could reshape the definition and classification of cell states, providing a physics-based complement to genomics and proteomics with implications from fundamental cell biology to precision medicine.

Methods

Diamond sensor preparation

The diamond substrate used in this work was a $50\,\mu\mathrm{m}$-thick, (111)-oriented diamond of natural isotopic abundance. Its surface layer was grown by chemical vapor deposition and isotopically purified to 99.99% ^{12}C to suppress spin-bath noise. NV centers were created by 60-keV $^{15}N^{+}$ ion implantation followed by annealing at 1000 $^{\circ}\mathrm{C}$. An array of etched micropillars (5-µm height, 5-µm diameter, 10-µm pitch) was fabricated on the diamond surface.

Experimental setup

The simplified experimental setup, illustrated in Fig. S1, can be divided into four main sections. The first part is microwave and radio-frequency system. Microwave control pulses for the NV centers were generated using an arbitrary waveform generator (AWG, Keysight M8190) and a PSG Vector Signal Generator (Keysight E8267D). The MW frequency was up-converted through an IQ modulator before being applied to NV center. For Overhauser DNP, a signal generator (HMC-T2220) delivered microwave excitation at the electron spin resonance frequency of TEMPOL. For RF control, two additional AWGs (Keysight 33522B and 33622A) generated independent pulse sequences. One addressed the NV's native nitrogen nuclear spin. Its output was combined with the microwave drive via a diplexer and delivered to the coplanar waveguide. The other drove a compact RF coil for ^{1}H manipulation through a home-built RLC circuit. All microwave and RF paths were amplified by separate power amplifiers before being applied to the sample. Laser excitation used 532- and 594-nm sources. Both beams were gated with acousto-optic modulators, combined using an RGB combiner, and directed by a dichroic beam splitter into an oil-immersion objective (Olympus, UPLAPO100XOHR) to focus onto the diamond. Photoluminescence from the NV centers was collected through the same objective, spectrally separated by the same dichroic, and detected with an avalanche photodiode. The real-time feedback and control unit consisted of a Zurich Instruments AWG and a PulseBlaster timing controller. During charge-state pre-selection, the AWG ran a photon-count-based feedback loop in which photon counts served as decision signals to proceed or restart, ensuring initialization to NV^{-}. The PulseBlaster synchronized all AWG channels, AOMs, and hardware triggers, controlling the timing of the entire experimental sequence. As shown in Fig. S1, the sample, coil, objective, and a single-sided magnet mounted on a translation stage were housed in a temperature-controlled enclosure to ensure magnetic-field and temperature stability during the experiments. The field homogeneity of the single-sided Halbach magnet is shown in Fig.

S5.

Cell preparation and mounting

MCF7 (ATCC HTB-22) and HeLa (ATCC CCL-2) cell lines were purchased from Pricella, authenticated by short tandem repeat (STR) analysis, and tested negative for mycoplasma. Cells were cultured in MEM (Pricella) supplemented with 10% fetal bovine serum (Vivacell) and 1% penicillin-streptomycin (HyClone) at $37\,^{\circ}\mathrm{C}$ in a humidified incubator with 5% CO_2. The MCF7 cultures were additionally supplemented with $10\,\mu\mathrm{g\,mL^{-1}}$ insulin. The cells were washed with phosphate-buffered saline (PBS), and then dissociated with trypsin (Thermo Fisher Scientific) to obtain a cell suspension. Subsequently, 100 mM TEMPOL in 1× HEPES buffer was added to the cell suspension at a 1:4 (v/v) ratio (buffer:cell suspension). The cell suspension was then dropped onto the waveguide structure and covered with the diamond. Afterwards, the assembly was rinsed three times with 20 mM TEMPOL in 1× HEPES buffer and sealed with wax. Finally the sample was mounted on the platform for measurement. A simplified schematic of the workflow is shown in Fig. S2.

Data processing

The raw fluorescence was acquired in two detection phases by alternating the final ENDOR readout pulse between $+\pi_y/2$ and $-\pi_y/2$, corresponding to N_+ and N_-. For each measurement, the signal contrast was defined as

$$C = \frac{N_+ - N_-}{N_+}, \tag{4}$$

which compensates for fluctuations in fluorescence. Each experiment comprised 70 repeats following a DNP sequence to abtain the T_1 relaxation data, and the entire measurement was repeated multiple times to improve the signal-to-noise ratio. For each individual cell, the experiment was performed over detuning values in the range of [-60,60] kHz. The central region

[-15,15] kHz was taken as the signal window, while the outer detuning points served as references. The baseline-corrected contrast was computed as

$$C_{\mathrm{corr}}(\tau) = \overline{C}_{\mathrm{win}}(\tau) - \overline{C}_{\mathrm{ref}}(\tau), \tag{5}$$

where $\overline{C}_{\mathrm{win}}(\tau)$ is the average over the window and $\overline{C}_{\mathrm{ref}}(\tau)$ is the average over the outer detuning points. The T_1 values were extracted by fitting the data to a single-exponential decay function:

$$C(\tau) = C_0 \sin(A * e^{-\tau/T_1}) \tag{6}$$

rather than a simple exponential decay, which reflects the detected NMR signal exceeds the linear regime. When the signal is sufficiently strong, the accumulated phase can exceed $\pi/2$, leading to an apparent inversion of the measured contrast.

Statistical analysis

The T_1 of MCF7 and Hela cells (T_1^{M} and T_1^{H}) were compared using the exact two-sided Mann-Whitney U test ($p = 0.0049$). Effect size was summarized with Cliff's delta ($\delta = 0.78$, 95% CI 0.40-1.00), with confidence limits obtained via nonparametric bootstrap resampling. We also reported the Hodges-Lehmann estimator of the median difference defined as ($T_1^{\mathrm{M}} - T_1^{\mathrm{H}}$) (estimate -36.5, 95% CI -52.5 to -8.5).

References

1. S. M. Rafelski, J. A. Theriot, Establishing a conceptual framework for holistic cell states and state transitions. *Cell* **187**, 2633–2651 (2024).

2. W. A. Lim, The emerging era of cell engineering: Harnessing the modularity of cells to program complex biological function. *Science* **378**, 848–852 (2022).

3. A. Regev, S. A. Teichmann, E. S. Lander, I. Amit, C. Benoist, E. Birney, B. Bodenmiller, P. Campbell, P. Carninci, M. Clatworthy, *et al.*, The human cell atlas. *elife* **6**, e27041 (2017).

4. M. Haniffa, D. Taylor, S. Linnarsson, B. J. Aronow, G. D. Bader, R. A. Barker, P. G. Camara, J. G. Camp, A. Chédotal, A. Copp, *et al.*, A roadmap for the human developmental cell atlas. *Nature* **597**, 196–205 (2021).

5. A. W. Wognum, A. C. Eaves, T. E. Thomas, Identification and isolation of hematopoietic stem cells. *Archives of medical research* **34**, 461–475 (2003).

6. M. R. Abbaszadegan, V. Bagheri, M. S. Razavi, A. A. Momtazi, A. Sahebkar, M. Gholamin, Isolation, identification, and characterization of cancer stem cells: A review. *Journal of cellular physiology* **232**, 2008–2018 (2017).

7. C. W. Shields Iv, C. D. Reyes, G. P. López, Microfluidic cell sorting: a review of the advances in the separation of cells from debulking to rare cell isolation. *Lab on a Chip* **15**, 1230–1249 (2015).

8. W. Bonner, H. Hulett, R. Sweet, L. Herzenberg, Fluorescence activated cell sorting. *Review of Scientific Instruments* **43**, 404–409 (1972).

9. L. A. Herzenberg, D. Parks, B. Sahaf, O. Perez, M. Roederer, L. A. Herzenberg, The history and future of the fluorescence activated cell sorter and flow cytometry: a view from Stanford. *Clinical chemistry* **48**, 1819–1827 (2002).

10. A. Baysoy, Z. Bai, R. Satija, R. Fan, The technological landscape and applications of single-cell multi-omics. *Nature Reviews Molecular Cell Biology* **24**, 695–713 (2023).

11. M. Frenea-Robin, J. Marchalot, Basic principles and recent advances in magnetic cell separation. *Magnetochemistry* **8**, 11 (2022).

12. S. A. Faraghat, K. F. Hoettges, M. K. Steinbach, D. R. Van Der Veen, W. J. Brackenbury, E. A. Henslee, F. H. Labeed, M. P. Hughes, High-throughput, low-loss, low-cost, and label-free cell separation using electrophysiology-activated cell enrichment. *Proceedings of the National Academy of Sciences* **114**, 4591–4596 (2017).

13. K. Inomata, A. Ohno, H. Tochio, S. Isogai, T. Tenno, I. Nakase, T. Takeuchi, S. Futaki, Y. Ito, H. Hiroaki, *et al.*, High-resolution multi-dimensional NMR spectroscopy of proteins in human cells. *Nature* **458**, 106–109 (2009).

14. L. Barbieri, E. Luchinat, L. Banci, Characterization of proteins by in-cell NMR spectroscopy in cultured mammalian cells. *Nature protocols* **11**, 1101–1111 (2016).

15. A. G. Palmer III, NMR characterization of the dynamics of biomacromolecules. *Chemical reviews* **104**, 3623–3640 (2004).

16. P. Glover, P. Mansfield, Limits to magnetic resonance microscopy. *Reports on progress in physics* **65**, 1489 (2002).

17. E. Luchinat, L. Banci, In-cell NMR: a topical review. *IUCrJ* **4**, 108–118 (2017).

18. F.-X. Theillet, E. Luchinat, In-cell NMR: Why and how? *Progress in Nuclear Magnetic Resonance Spectroscopy* **132**, 1–112 (2022).

19. G. Sivelli, A. Barakat, K. B. Marable, G. Gruet, S. L. Bitetti, B. Behr, V. Lodde, A. M. Luciano, C. Herrera, M. Blom, *et al.*, Micro magnetic resonance spectroscopy for noninvasive metabolic screening of mammalian embryos and oocytes. *Proceedings of the National Academy of Sciences* **122**, e2424459122 (2025).

20. T. Wolf, P. Neumann, K. Nakamura, H. Sumiya, T. Ohshima, J. Isoya, J. Wrachtrup, Subpicotesla diamond magnetometry. *Physical Review X* **5**, 041001 (2015).

21. K. Fang, V. M. Acosta, C. Santori, Z. Huang, K. M. Itoh, H. Watanabe, S. Shikata, R. G. Beausoleil, High-sensitivity magnetometry based on quantum beats in diamond nitrogen-vacancy centers. *Physical review letters* **110**, 130802 (2013).

22. K. Arai, C. Belthangady, H. Zhang, N. Bar-Gill, S. DeVience, P. Cappellaro, A. Yacoby, R. L. Walsworth, Fourier magnetic imaging with nanoscale resolution and compressed sensing speed-up using electronic spins in diamond. *Nature nanotechnology* **10**, 859–864 (2015).

23. Z. Zhao, X. Ye, S. Xu, P. Yu, Z. Yang, X. Kong, Y. Wang, T. Xie, F. Shi, J. Du, Sub-nanotesla sensitivity at the nanoscale with a single spin. *National Science Review* **10**, nwad100 (2023).

24. J. Du, F. Shi, X. Kong, F. Jelezko, J. Wrachtrup, Single-molecule scale magnetic resonance spectroscopy using quantum diamond sensors. *Reviews of Modern Physics* **96**, 025001 (2024).

25. H. Mamin, M. Kim, M. Sherwood, C. T. Rettner, K. Ohno, D. Awschalom, D. Rugar, Nanoscale nuclear magnetic resonance with a nitrogen-vacancy spin sensor. *Science* **339**, 557–560 (2013).

26. T. Staudacher, F. Shi, S. Pezzagna, J. Meijer, J. Du, C. A. Meriles, F. Reinhard, J. Wrachtrup, Nuclear magnetic resonance spectroscopy on a (5-nanometer)^3 sample volume. *Science* **339**, 561–563 (2013).

27. I. Lovchinsky, A. Sushkov, E. Urbach, N. P. de Leon, S. Choi, K. De Greve, R. Evans, R. Gertner, E. Bersin, C. Müller, *et al.*, Nuclear magnetic resonance detection and spectroscopy of single proteins using quantum logic. *Science* **351**, 836–841 (2016).

28. F. Shi, Q. Zhang, P. Wang, H. Sun, J. Wang, X. Rong, M. Chen, C. Ju, F. Reinhard, H. Chen, *et al.*, Single-protein spin resonance spectroscopy under ambient conditions. *Science* **347**, 1135–1138 (2015).

29. N. Aslam, M. Pfender, P. Neumann, R. Reuter, A. Zappe, F. Fávaro de Oliveira, A. Denisenko, H. Sumiya, S. Onoda, J. Isoya, *et al.*, Nanoscale nuclear magnetic resonance with chemical resolution. *Science* **357**, 67–71 (2017).

30. S. Schmitt, T. Gefen, F. M. Stürner, T. Unden, G. Wolff, C. Müller, J. Scheuer, B. Naydenov, M. Markham, S. Pezzagna, *et al.*, Submillihertz magnetic spectroscopy performed with a nanoscale quantum sensor. *Science* **356**, 832–837 (2017).

31. D. R. Glenn, D. B. Bucher, J. Lee, M. D. Lukin, H. Park, R. L. Walsworth, High-resolution magnetic resonance spectroscopy using a solid-state spin sensor. *Nature* **555**, 351–354 (2018).

32. V. Proserpio, T. Lönnberg, Single-cell technologies are revolutionizing the approach to rare cells. *Immunology and cell biology* **94**, 225–229 (2016).

33. Y. Chen, P. Li, P.-H. Huang, Y. Xie, J. D. Mai, L. Wang, N.-T. Nguyen, T. J. Huang, Rare cell isolation and analysis in microfluidics. *Lab on a Chip* **14**, 626–645 (2014).

34. R. A. Beckman, G. S. Schemmann, C.-H. Yeang, Impact of genetic dynamics and single-cell heterogeneity on development of nonstandard personalized medicine strategies for cancer. *Proceedings of the National Academy of Sciences* **109**, 14586–14591 (2012).

35. A. K. Dutta, J.-B. Alberge, R. Sklavenitis-Pistofidis, E. D. Lightbody, G. Getz, I. M. Ghobrial, Single-cell profiling of tumour evolution in multiple myeloma—opportunities for precision medicine. *Nature Reviews Clinical Oncology* **19**, 223–236 (2022).

36. D. Jovic, X. Liang, H. Zeng, L. Lin, F. Xu, Y. Luo, Single-cell RNA sequencing technologies and applications: A brief overview. *Clinical and translational medicine* **12**, e694 (2022).

37. S. S. Potter, Single-cell RNA sequencing for the study of development, physiology and disease. *Nature Reviews Nephrology* **14**, 479–492 (2018).

38. S. Han, X. Ye, X. Zhou, Z. Liu, Y. Guo, M. Wang, W. Ji, Y. Wang, J. Du, Solid-state spin coherence time approaching the physical limit. *Science Advances* **11**, eadr9298 (2025).

39. D. A. Hopper, J. D. Lauigan, T.-Y. Huang, L. C. Bassett, Real-time charge initialization of diamond nitrogen-vacancy centers for enhanced spin readout. *Physical Review Applied* **13**, 024016 (2020).

40. T. Xie, Z. Zhao, X. Kong, W. Ma, M. Wang, X. Ye, P. Yu, Z. Yang, S. Xu, P. Wang, *et al.*, Beating the standard quantum limit under ambient conditions with solid-state spins. *Science Advances* **7**, eabg9204 (2021).

41. P. Neumann, J. Beck, M. Steiner, F. Rempp, H. Fedder, P. R. Hemmer, J. Wrachtrup, F. Jelezko, Single-shot readout of a single nuclear spin. *Science* **329**, 542–544 (2010).

42. T. R. Carver, C. P. Slichter, Experimental verification of the Overhauser nuclear polarization effect. *Physical Review* **102**, 975 (1956).

43. D. B. Bucher, D. R. Glenn, H. Park, M. D. Lukin, R. L. Walsworth, Hyperpolarization-enhanced NMR spectroscopy with femtomole sensitivity using quantum defects in diamond. *Physical Review X* **10**, 021053 (2020).

44. R. Damadian, Tumor detection by nuclear magnetic resonance. *Science* **171**, 1151–1153 (1971).

45. Ş. Comşa, A. M. Cimpean, M. Raica, The story of MCF-7 breast cancer cell line: 40 years of experience in research. *Anticancer research* **35**, 3147–3154 (2015).

46. J. R. Masters, HeLa cells 50 years on: the good, the bad and the ugly. *Nature Reviews Cancer* **2**, 315–319 (2002).

47. G. Fullerton, I. Cameron, V. Ord, Frequency dependence of magnetic resonance spin-lattice relaxation of protons in biological materials. *Radiology* **151**, 135–138 (1984).

48. P. A. Bottomley, T. H. Foster, R. E. Argersinger, L. M. Pfeifer, A review of normal tissue hydrogen NMR relaxation times and relaxation mechanisms from 1–100 MHz: dependence on tissue type, NMR frequency, temperature, species, excision, and age. *Medical physics* **11**, 425–448 (1984).

49. P. A. Bottomley, C. Hardy, R. Argersinger, G. Allen-Moore, A review of ^{1}H nuclear magnetic resonance relaxation in pathology: are T_1 and T_2 diagnostic? *Medical physics* **14**, 1–37 (1987).

50. S. H. Koenig, Molecular basis of magnetic relaxation of water protons of tissue. *Academic radiology* **3**, 597–606 (1996).

51. M. Gaeta, M. Cavallaro, S. L. Vinci, E. Mormina, A. Blandino, M. A. Marino, F. Granata, A. Tessitore, K. Galletta, T. D'Angelo, *et al.*, Magnetism of materials: theory and practice in magnetic resonance imaging. *Insights into Imaging* **12**, 179 (2021).

52. S. H. Koenig, R. D. Brown III, Field-cycling relaxometry of protein solutions and tissue: implications for MRI. *Progress in Nuclear Magnetic Resonance Spectroscopy* **22**, 487–567 (1990).

53. R. Henkelman, G. Stanisz, S. Graham, Magnetization transfer in MRI: a review. *NMR in Biomedicine: An International Journal Devoted to the Development and Application of Magnetic Resonance In Vivo* **14**, 57–64 (2001).

54. W. R. Nitz, P. Reimer, Contrast mechanisms in MR imaging. *European radiology* **9**, 1032–1046 (1999).

55. G. M. Whitesides, The origins and the future of microfluidics. *Nature* **442**, 368–373 (2006).

56. T. M. Squires, S. R. Quake, Microfluidics: Fluid physics at the nanoliter scale. *Reviews of modern physics* **77**, 977–1026 (2005).

57. R. D. Allert, F. Bruckmaier, N. R. Neuling, F. A. Freire-Moschovitis, K. S. Liu, C. Schrepel, P. Schätzle, P. Knittel, M. Hermans, D. B. Bucher, Microfluidic quantum sensing platform for lab-on-a-chip applications. *Lab on a Chip* **22**, 4831–4840 (2022).

Acknowledgements

We thank Dominik B. Bucher for his valuable suggestions on the use of hyperpolarization techniques. **Funding:** This work was supported by the Chinese Academy of Sciences (Grants No. YSBR-068), the National Natural Science Foundation of China (Grants No. T2125011, No. 12274396, No. 12404555), Innovation Program for Quantum Science and Technology (Grants No. 2021ZD0302200, 2021ZD0303204), the China Postdoctoral Science Foundation (Grants No. 2021M703110, No. 2022T150631, No. 2023M743399, No. 2024M753084), the Postdoctoral Fellowship Program of CPSF (Grants No. GZB20240717, No. GZB20240718), and the Fundamental Research Funds for the Central Universities, New Cornerstone Science Foundation through the XPLORER PRIZE. **Author contributions:** J.D. and F.S. supervised the project and proposed the idea. Z.Z., F.S. and J.D. designed the experiments. Z.Z., Q.S., S.X. and T.X. prepared the setup. X.Y. and Y.W. prepared the diamond sample. Q.S. and J.S. prepared the cell samples. Z.Z., Q.S. and S.X. performed the experiment and the simulation. Q.S. and Z.Z. performed the primary data acquisition. Z.Z., Q.S., Q.H., F.S. and J.D. wrote the manuscript. All authors analysed the data, discussed the results and commented on the manuscript. **Competing interests:** The authors declare that they have no competing interests. **Data and materials availability:** All data needed to evaluate the conclusions in the paper are present in the paper and/or the Supplementary Materials.

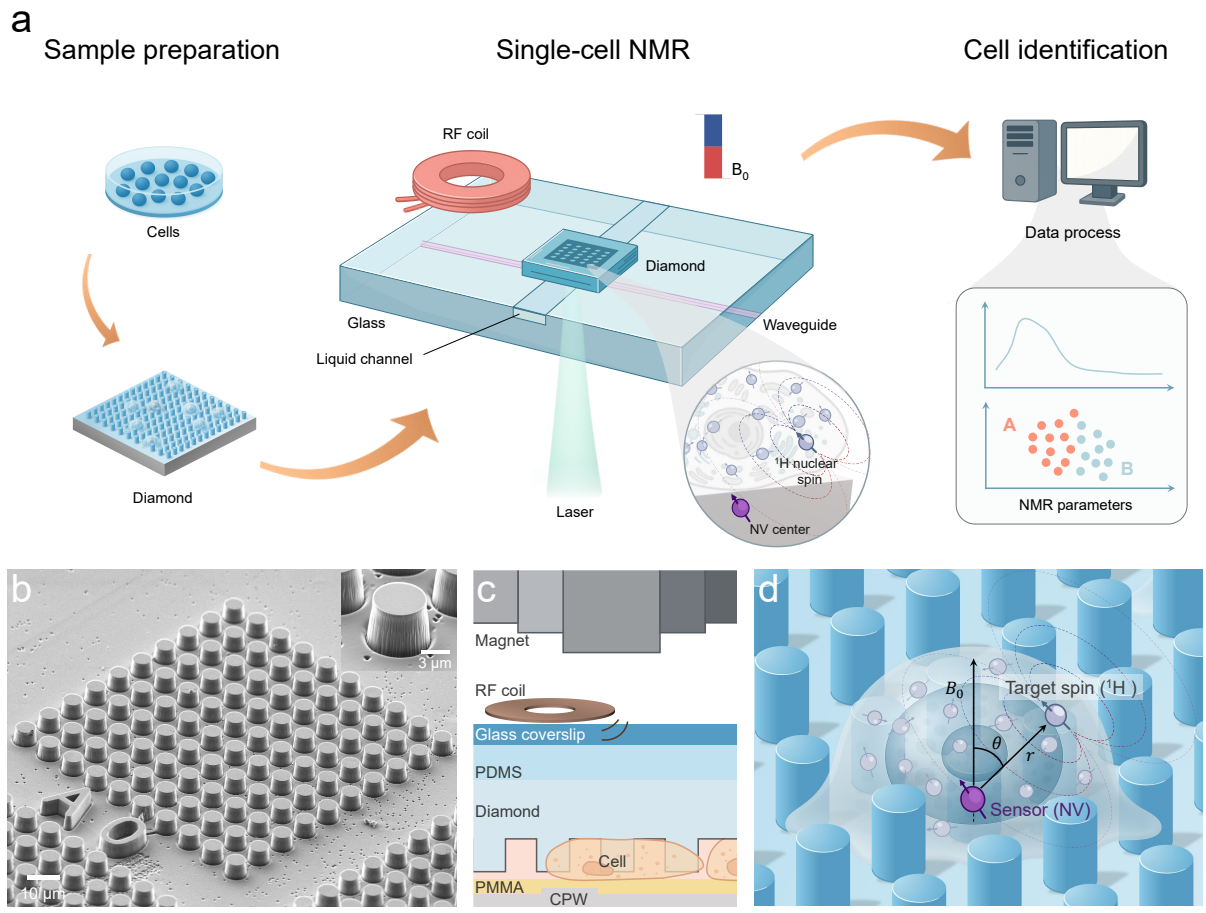

Fig. 1. NV-enhanced single-cell NMR for label-free cell identification. (a) Single-cell identification workflow. Individual cells are measured with NV-enhanced NMR, where NMR contrasts such as proton spin-lattice relaxation enable label-free discrimination of cell types. A diamond-based microfluidic chip with a liquid channel is aligned below a diamond hosting near-surface NV centers and a microstructured surface region. NV spins are optically initialized and read out with laser pulses. Microwaves, delivered via a coplanar waveguide, drive the NV electron spin, while a radio-frequency (RF) coil addresses intracellular ^{1}H nuclei . A static magnetic field B_0 sets the quantization axis. Time-domain signals are processed to extract quantitative NMR parameters, which serve as features for label-free classification. (b) Scanning electron micrograph of the diamond pillar array. Inset, higher-magnification view of a single diamond pillar. (c) Cross-sectional schematic of the single-cell NMR chip, showing the magnet, RF coil, glass coverslip, polydimethylsiloxane (PDMS) layer, diamond with pillar array, polymethyl methacrylate (PMMA) support and coplanar waveguide (CPW). Further structural details are provided in the Supplementary Information. (d) Principle of NV-based single-cell NMR, where an NV sensor in a diamond pillar detects the nuclear spins (^{1}H) of a single cell under an external magnetic field. Enlarged view of the dipolar interaction between an NV spin and nuclear spins within a cell. The interaction depends on the NV-nucleus separation r and the relative angle θ to magnetic field (see Supplementary Information).

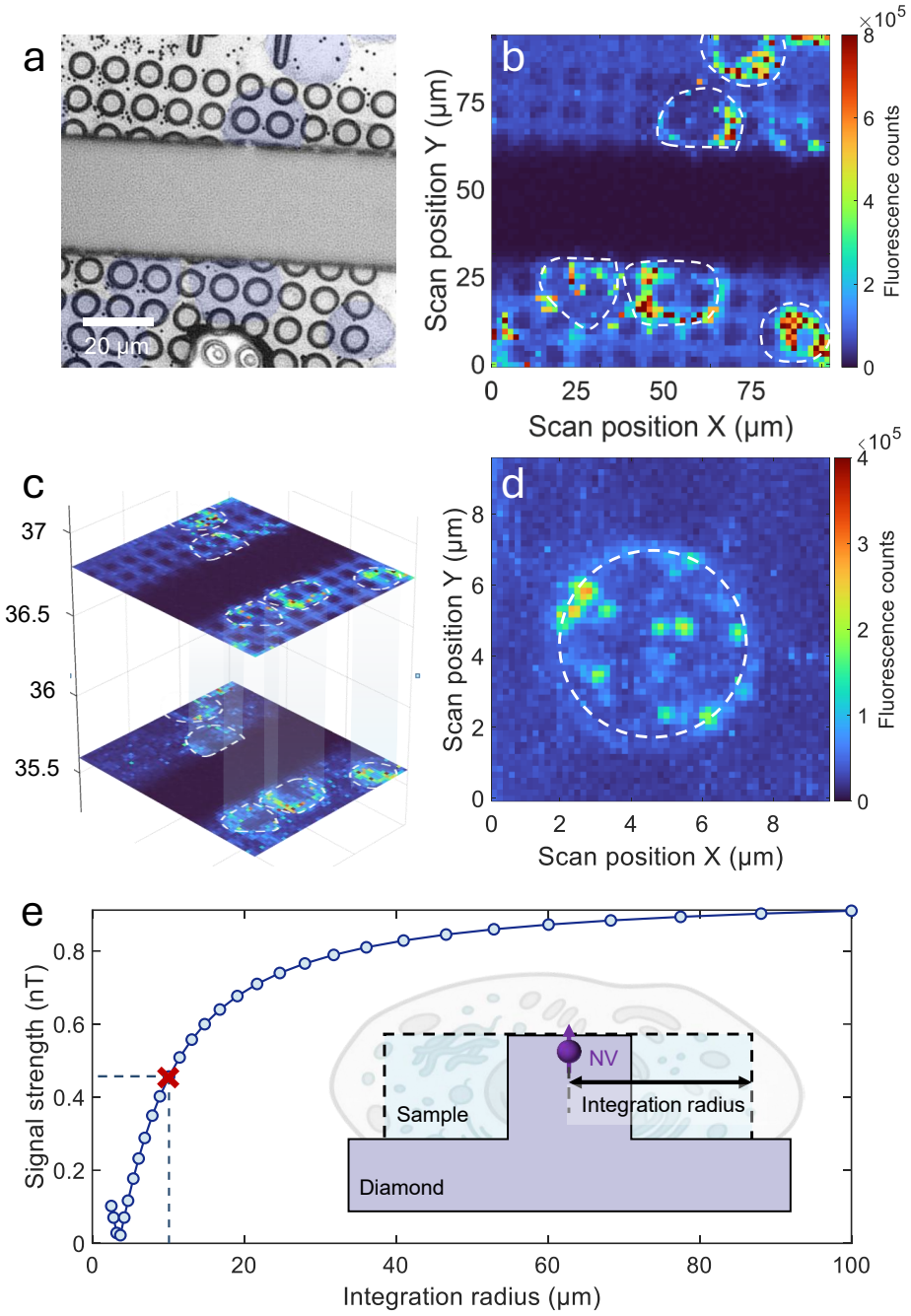

Fig. 2. Localization of the detected NMR signal to a single cell. (a) Optical micrograph of the diamond pillar array with cells sealed on top. Cells are highlighted with a blue pseudo-color overlay and the central band corresponds to the CPW. (b) NV fluorescence scan of the same region as a function of the lateral scan position, with dashed contours indicating the positions of individual cells. (c) Three-dimensional stack of NV fluorescence images at different focal planes, showing that the fluorescence contrast is confined to the NV pillars located beneath a single cell. (d) Zoom-in of the NV fluorescence map around one selected pillar used for single-cell measurements. (e) Integrated NMR signal strength as a function of the lateral integration radius around the NV sensor. The red marker indicates the radius at which half of the total signal is accumulated and the signal saturates for radii comparable to the cell size, demonstrating that the detected NMR signal is dominated by nuclear spins within a single cell.

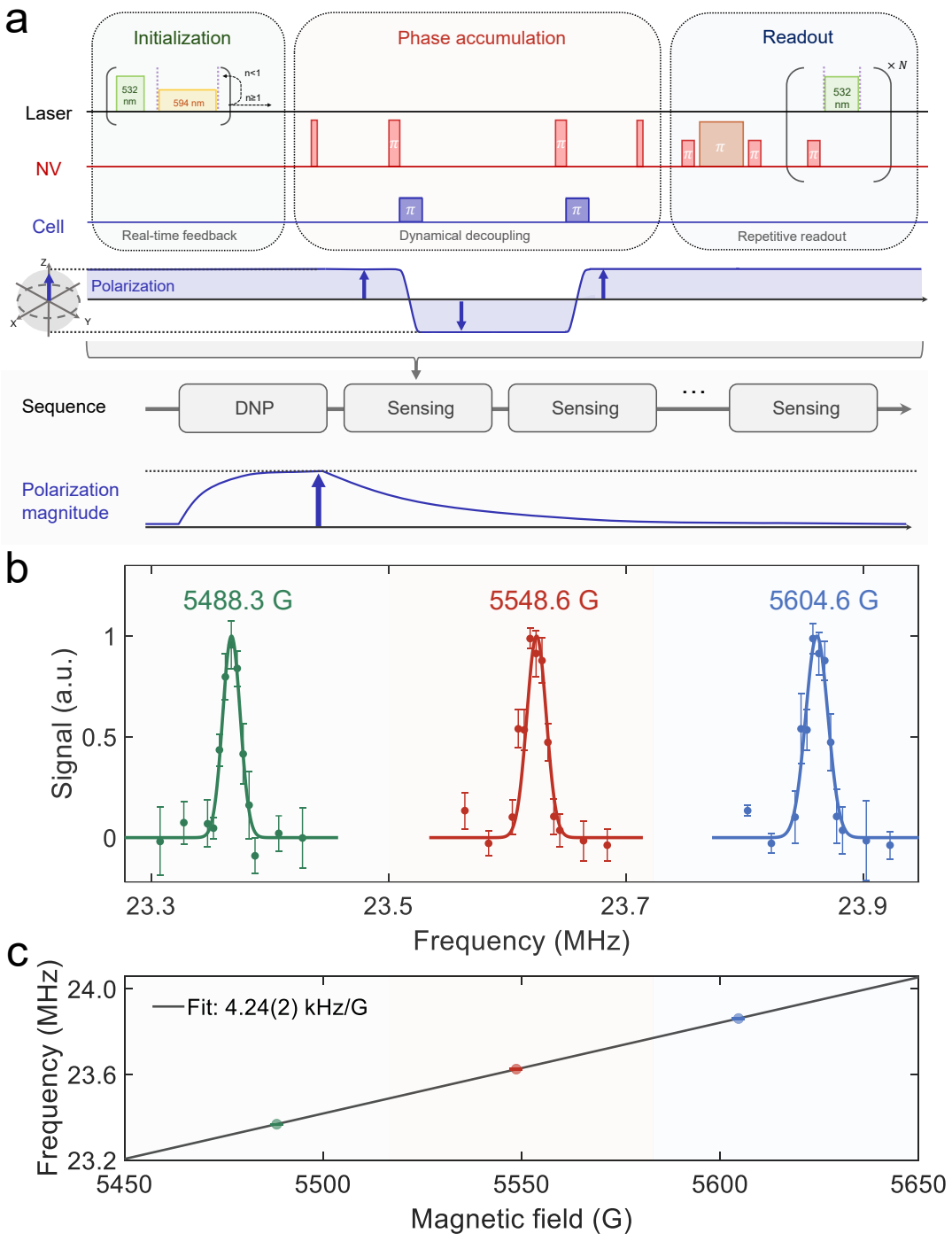

Fig. 3. Single-cell NMR detection and identification of proton signals. (a) Top: The detection sequence consists of three parts: initialization with real-time feedback charge-state preparation, the ENDOR sequence with dynamical decoupling, and readout via SWAP operations that transfer the electron state to the nuclear spin for repetitive readout. Bottom: The full experiment begins with DNP to build nuclear polarization, followed by repeated sensing cycles. Polarization is sampled in each cycle and relaxes between cycles toward Boltzmann equilibrium with T_1. (b) Proton resonance spectra obtained at different magnetic fields, with the horizontal axis showing the applied RF frequency. Solid lines are fits to the data. (c) Linear fit of resonance frequency versus magnetic field yields a slope of 4.24(2) kHz/G, in agreement with the proton gyromagnetic ratio (4.26 kHz/G).

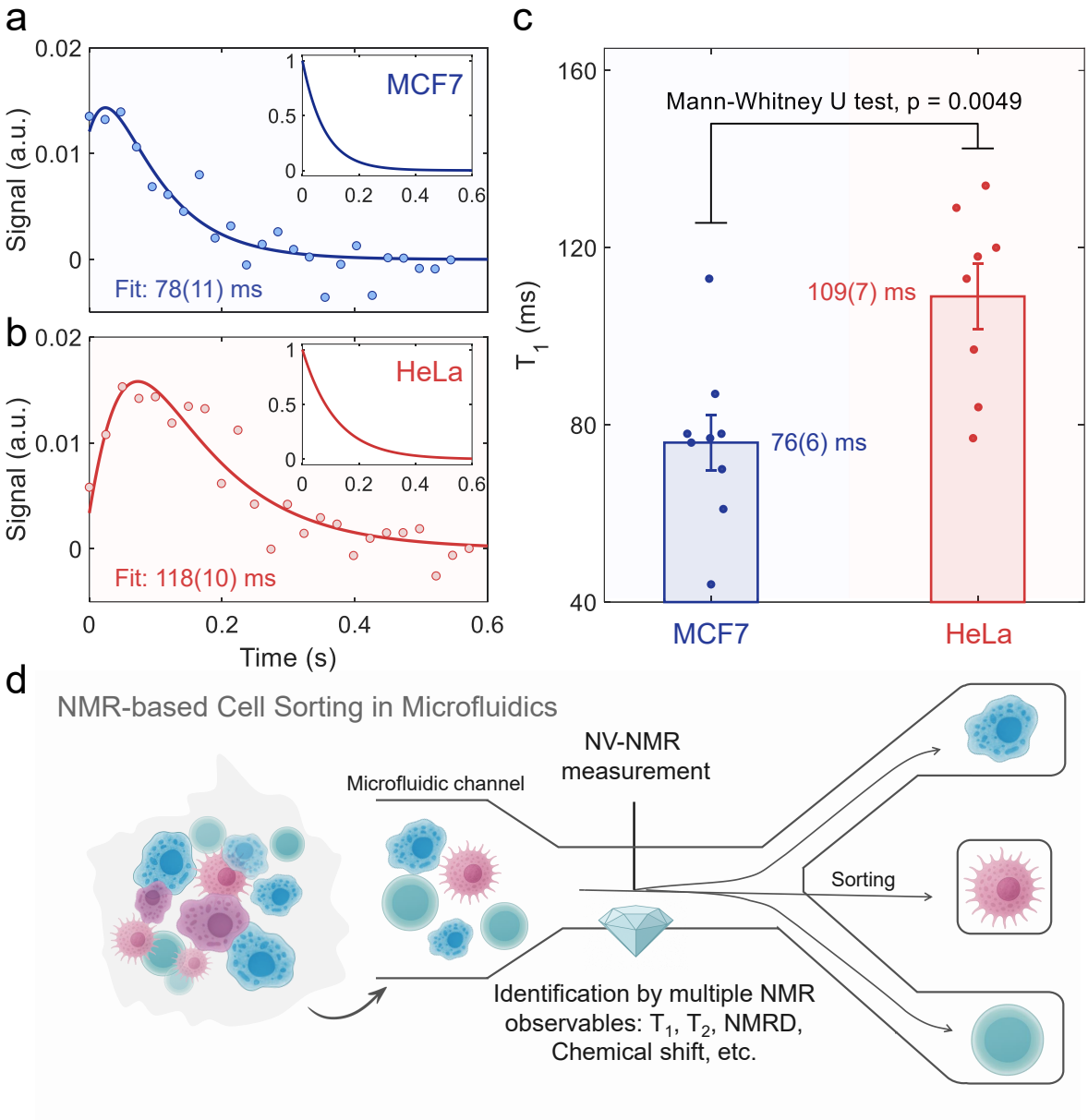

Fig. 4. Measurement and statistical analysis of single-cell relaxation times for label-free cell identification. (a) Representative T_1 relaxation curves for an individual MCF7 cell. Markers show a three-point moving average of the raw signal. Because the detected NMR signal exceeds the linear regime, solid curves are fits to the function $C_0 \sin(Ae^{-t/T_1})$. The inset shows the reconstructed polarization decay $P(t) \propto e^{-t/T_1}$. (b) Representative T_1 relaxation curves for an individual HeLa cell. (c) Statistical comparison of nuclear relaxation times. Population statistics of T_1 show a significant difference between MCF7 and HeLa cells ($p = 0.0049$, Mann-Whitney U test), with a large effect size (Cliff's $\delta = 0.78$) and a median T_1 difference of about 36.5 ms (Hodges-Lehmann estimator). Mean T_1 values are $76(6)$ ms for MCF7 and $109(7)$ ms for HeLa. (d) Envisioned multi-parametric single-cell analysis with NMR-based microfluidics. Cells flow through microfluidic channels into an NV-based detection region, where intrinsic NMR signatures (T_1, T_2, chemical shift, NMRD) are measured for label-free identification and sorting. This platform can be extended to high-throughput analysis and integration with other single-cell omics.

Supplementary information for Single-cell identification with quantum-enhanced nuclear magnetic resonance

EXPERIMENTAL DETAILS

Sample assembly

The diamond was pre-cleaned in a tri-acid mixture at 180 °C for 4 hours. It was then supported by a 300 µm Polydimethylsiloxane (PDMS) film attached to a 170 µm glass substrate, giving a total stack thickness of ∼520 µm. This relatively thin configuration ensured close proximity to the RF coil above the glass (Fig. S1b), enabling a sufficiently strong driving field for nuclear-spin manipulation. The compliant PDMS layer between the diamond and glass allowed the diamond micropillars to gently compress the cell sample, positioning single cells to wrap around individual pillars. In addition, the diamond surface was coated with a monolayer of graphene (ACS Material), which quenched background fluorescence via fluorescence resonance energy transfer.

The glass microfluidic channel was bonded directly onto the coplanar waveguide (CPW) using a UV-curable adhesive, giving an overall thickness of ∼300 µm. To minimize microwave absorption in water and maintain strong driving fields at high frequencies, the CPW surface was coated with PMMA (A7, ALMAAK, Germany). The coating was prepared by spin-coating at 2000 rpm, forming a uniform 3 µm protective layer. This treatment substantially reduced dielectric losses, thereby maintaining efficient microwave delivery to the sample.

Pulse sequence

As shown in Fig. S3, the experimental sequence comprises five stages. Prior to the measurement sequence, dynamic nuclear polarization (DNP) of TEMPOL electron spins was performed via microwave irradiation delivered through the CPW. To suppress microwave heating effects, we applied microwaves with a duty cycle of 38% rather than continuous operation. This step established robust nuclear-spin polarization before NV-based detection.

In the initialization stage, the NV charge state was prepared with 532 nm and 594 nm laser pulses combined with real-time feedback, increasing the NV^- to over 90%. The measurement stage is based on an ENDOR sequence. The π and $\pi/2$ pulses were designed with the GRAPE algorithm (details in Fig. S6 and Fig. S7). At high fields, the nitrogen spin is essentially unpolarized, so driving all hyperfine sublevels would ordinarily require large power, which is challenging for a CPW. Shaped pulses achieve simultaneous addressing of all sublevels and

high-fidelity rotations at substantially lower drive. Following each NV π pulse, a π pulse is immediately applied to the protons. These nuclear inversions were implemented using optimized adiabatic control.

In the final readout stage, the electronic state is transferred to the nuclear spin, enabling repetitive readout of the nuclear spin state. The selective electron-spin drive was set to $\Omega = \delta/\sqrt{3}$ (with δ the hyperfine coupling), thereby eliminating flips of neighbouring hyperfine subspaces.

Calibration of the RF field

The transverse drive field B_x was calibrated for each cell using the Bloch–Siegert effect. The calibration pulse sequence is shown in Fig. S4. The measured contrast as a function of the applied RF voltage V was fitted to

$$C = C_0 \sin(K B_x^2 \tau) = C_0 \sin(K b_x^2 V^2 \tau), \tag{1}$$

where τ is the RF irradiation time in the sequence, $B_x = b_x V$ defines the RF field-voltage conversion factor b_x, and

$$K = \frac{\gamma_e^2}{2(D - \gamma_e B)} + \frac{\gamma_e^2}{4(D + \gamma_e B)} \tag{2}$$

is the Bloch–Siegert coefficient for the NV spin. The fit yields the conversion from RF drive voltage to B_x. We then set $B_x = 8$ G for subsequent single-cell NMR measurements.

NUMERICAL SIMULATIONS

Hamiltonian of the coupled NV-nuclear spin system

Single-cell nuclear magnetic resonance exploits the magnetic dipolar interaction between these nuclear spins and NV electronic spins. Under an external magnetic field applied along the NV axis, the Hamiltonian of the coupled NV-nuclear spin system can be expressed as

$$H = \underbrace{D S_z^2 + \gamma_e B_0 S_z}_{H_{\mathrm{NV}}} + \underbrace{\mathbf{S}_z \sum_j^N \left(a_{\parallel,j} I_{z,j} + a_{\perp,j} I_{\perp,j} \right)}_{H_{\mathrm{NV,nuclear}}} + \underbrace{\gamma_n B_0 \sum_j^N I_{z,j}}_{H_{\mathrm{nuclear}}}, \tag{3}$$

where D is the zero-field splitting, γ_e and γ_n are the electronic and nuclear gyromagnetic ratios, S_z denotes the NV electron spin operator, and $I_{z,j}, I_{\perp,j}$ are the spin components of

the j-th nucleus with hyperfine couplings $a_{\parallel,j}, a_{\perp,j}$. Here $I_\perp = \cos\phi I_x + \sin\phi I_y$, where ϕ and θ denote the azimuthal and polar angles between the NV axis and the nuclear spin. Neglecting Fermi contact terms, the longitudinal and transverse dipolar coupling strengths are given by

$$\begin{aligned} a_\parallel &= \frac{\mu_0 \gamma_e \gamma_n \hbar}{4\pi r^3}(3\cos^2\theta - 1), \\ a_\perp &= \frac{\mu_0 \gamma_e \gamma_n \hbar}{4\pi r^3}\, 3\sin\theta\cos\theta. \end{aligned} \tag{4}$$

These couplings can equivalently be interpreted as effective static and oscillating magnetic fields parallel and perpendicular to the NV axis, respectively. Both components are accessible to NV-based detection. In this work, we employ an electron-nuclear double resonance (ENDOR) sequence to probe the longitudinal component.

Effective sensing volume

Given the weak coupling between the NV and nuclear spins, a semiclassical description is appropriate and the longitudinal component can be treated as an effective static field parallel to the NV axis. The magnetic field produced by a single nuclear spin has magnitude

$$b_\parallel = \frac{\mu_0 \gamma_n \hbar}{8\pi r^3}(3\cos^2\theta - 1). \tag{5}$$

To simulate NMR signal strength, we consider a uniformly distributed ensemble of nuclear spins with polarization P under an external magnetic field. The NV center is located at (0, 0, 5 μm), corresponding to the top of the pillar. For an ENDOR sequence with an evolution time τ, the phase accumulated by the NV spin is

$$\varphi = P\gamma_e \tau \sum_j b_{\parallel,j}. \tag{6}$$

The strength of the polarization signal depends on the sample geometry, and we evaluate it numerically by integrating over the sample volume according to Eq. (2). At B_0 = 5600 G and a temperature of 300 K, the Boltzmann thermal polarization of protons is $P \approx 1.9 \times 10^{-6}$. Space was discretized on a cubic grid with voxel size of 100 nm. Since the cells are compressed, the top of the pillar is in near contact with the radiating structure, as illustrated in Fig. S1. By varying the integration radius in the lateral plane, we calculated the polarization field at the NV position. The simulated dependence of the field magnitude

on the integration radius is shown in Fig. 2e. The results indicate that the field strength approaches a saturation value of ≈ 0.9 nT as the integration range tends to infinity. For a finite range of 10 µm, the field strength is about 0.45 nT. Given that a typical cell has a diameter of about 20 µm, the majority of the detected NMR signal originates from intracellular protons. With DNP, the signal strength is enhanced by more than an order of magnitude relative to thermal polarization.

Adiabatic RF control

To improve the control fidelity of proton spins, we used adiabatic inversion pulses rather than square pulses. The pulses were designed following the Landau–Zener model, ensuring adiabatic inversion over RF amplitude and detuning inhomogeneities. Specifically, we implemented a sinusoidal amplitude envelope together with a linear frequency sweep from -35 kHz to +35 kHz. Simulations (Fig. S8) confirm high-fidelity robustness of the adiabatic π pulses to RF-amplitude and detuning variations. This enhanced robustness is particularly advantageous for cellular relaxation-time measurements, where it mitigates control-induced acceleration of relaxation.

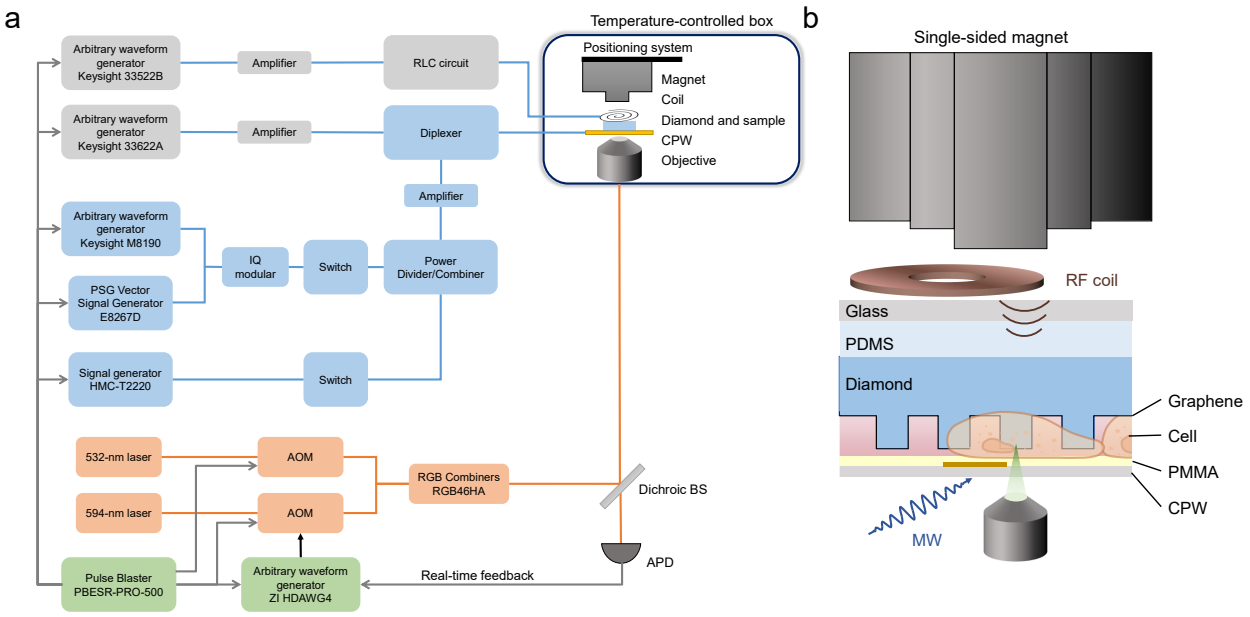

FIG. S1. **Experimental setup and sample architecture.** (a) Simplified experimental setup. The setup mainly consists of microwave (MW) and radio-frequency (RF) circuits (blue), optical systems (orange), synchronization and real-time feedback system (green), and a diamond platform inside a temperature-controlled box. MW control is generated by an arbitrary-waveform generator (AWG) and up-converted with a vector signal generator via IQ modulation. RF control is provided by two AWGs, amplified and either fed through an RLC circuit to a coil or combined with the MW path by a diplexer before delivery to a coplanar waveguide (CPW). Optical excitation (532 and 594 nm) is gated by AOMs and combined (RGB combiner), then directed through a dichroic beamsplitter (BS) and objective. NV photoluminescence is detected on an APD. A PulseBlaster timing controller and a Zurich Instruments AWG provide real-time feedback and hardware synchronization. The positioning system, magnet, RF coil, sample, CPW and objective are housed in a temperature-controlled enclosure. (b) Cross-section of the sample stack. A single-sided combined magnet provides the static field. An RF coil sits above a glass slide, which overlays a PDMS layer supporting the diamond with a micropillar array. Cells are compressed so that they wrap around individual pillars. A monolayer of graphene on the diamond quenches background fluorescence, while a PMMA coating on the coplanar waveguide (CPW) reduces dielectric loss and water absorption.

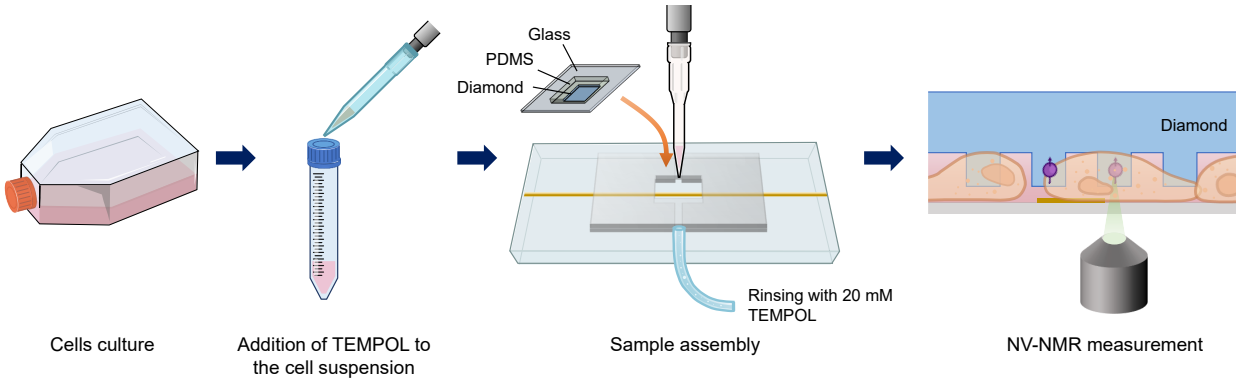

FIG. S2. **Workflow for single-cell NV-NMR measurement.** Schematic of sample preparation and measurement: (i) Cells are cultured. (ii) TEMPOL is added to the cell suspension. (iii) The sample is assembled by placing a PDMS-supported diamond on a glass coverslip and the diamond's micropillars gently compress the cells so that individual cells wrap around pillars. (iv) NV-NMR is performed through the objective.

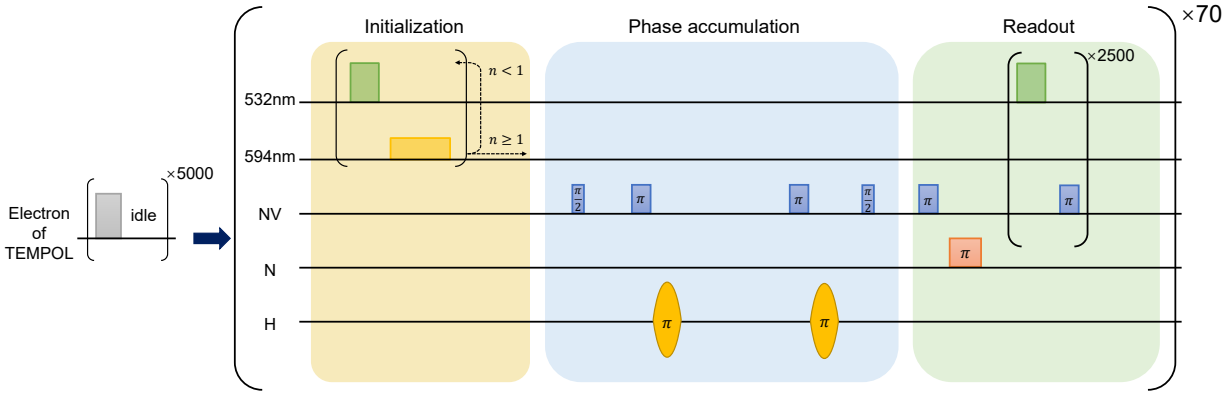

FIG. S3. **Pulse sequence for single-cell NMR.** Left: Overhauser DNP of TEMPOL electrons (microwave on/off) is repeated 5000 times, yielding an effective microwave on-time of 125 ms. Initialization: 532 and 594 nm pulses, with real-time feedback, prepare the NV in the negative charge state and the $|0\rangle$ spin state. Phase accumulation: the NV electron spin is driven by a CPMG-2 with shaped pulses. After each NV π pulse a nuclear π pulse (adiabatic) is applied on protons. Readout: the NV phase is mapped to the nitrogen spin and read out. The entire measurement cycle is executed 70 times.

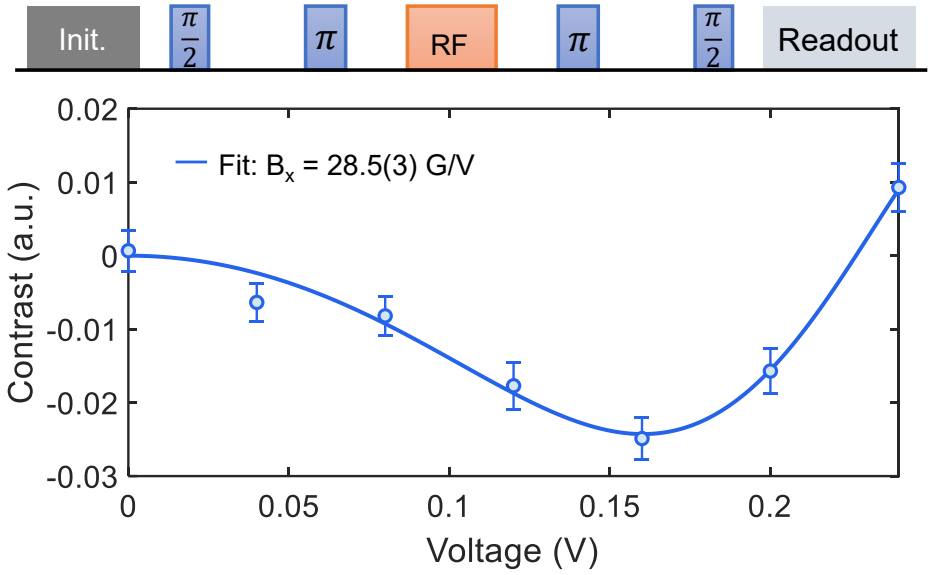

FIG. S4. **Calibration of the transverse RF field.** Top: calibration sequence used to measure the Bloch-Siegert shift. Bottom: contrast versus applied RF voltage. The solid line is a fit to $C = C_0 \sin(K(b_x V)^2 \tau)$, which yields $b_x = 28.5(3)$ G/V. We set B_x=8 G for subsequent single-cell NMR measurements.

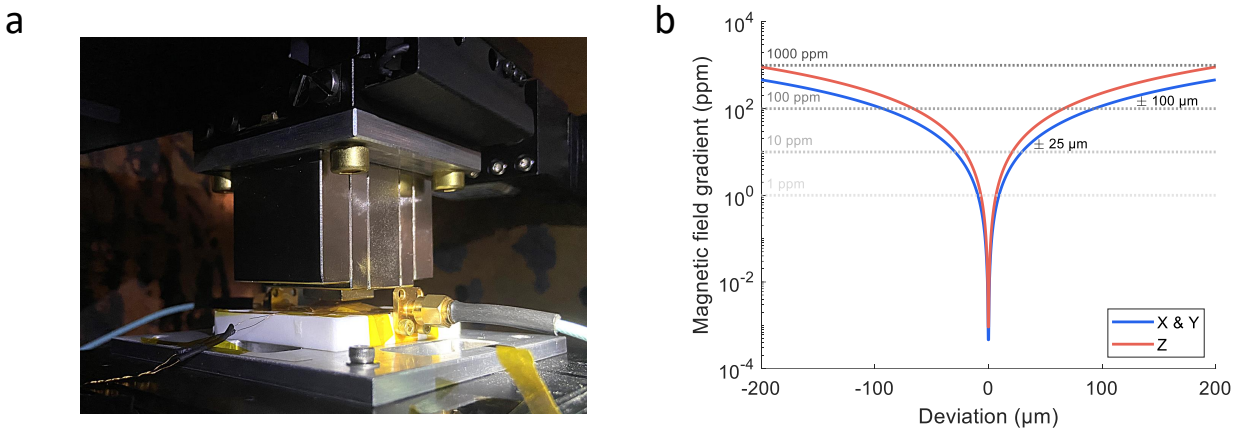

FIG. S5. **Single-sided Halbach magnet and field homogeneity.** (a) Photograph of the single-sided Halbach magnet assembly that provides the static field above the CPW/sample stack. (b) Magnetic-field homogeneity (shown as gradient in ppm) versus positional deviation. The red trace shows the axial (Z) homogeneity and the blue trace shows the lateral (X/Y) homogeneity. The shaded lines indicate typical levels. A homogeneous region of roughly ±25μm at ∼10 ppm is highlighted. Gradients were obtained by measuring the magnetic field at multiple positions.

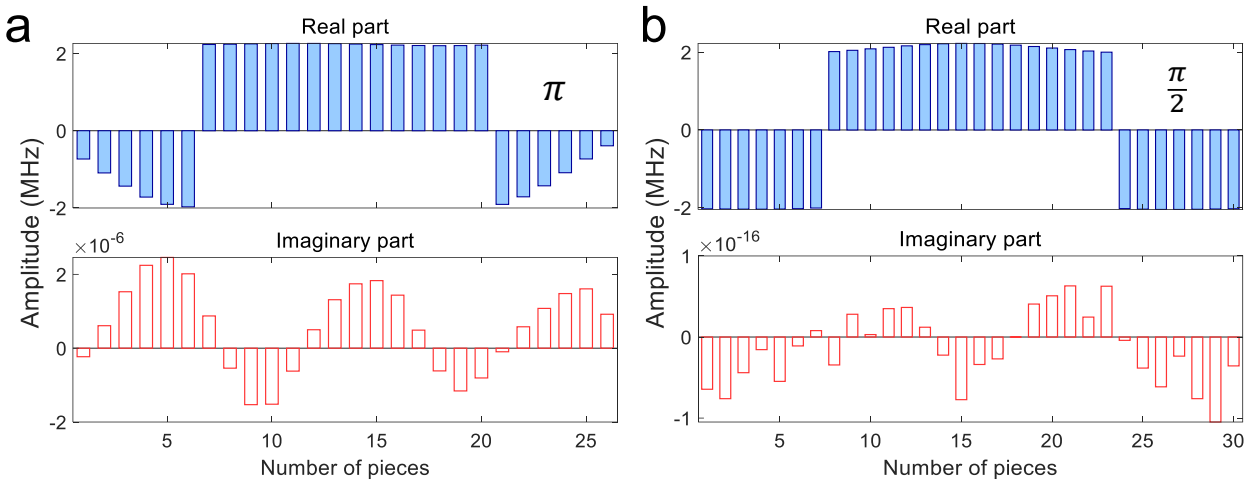

FIG. S6. **Optimal control for ^{15}N NV centers.** (a) The pulse sequence of the real (upper) and imaginary (lower) parts of the π pulses used in dynamical decoupling sequences and repetitive readout. The amplitude for each piece is denoted by Rabi frequency. Each piece lasts for 20 ns with 26 pieces in total. (b) The pulse sequence of the real (upper) and imaginary (lower) parts of the $\pi/2$ pulses. Each piece lasts for 20 ns with 30 pieces in total.

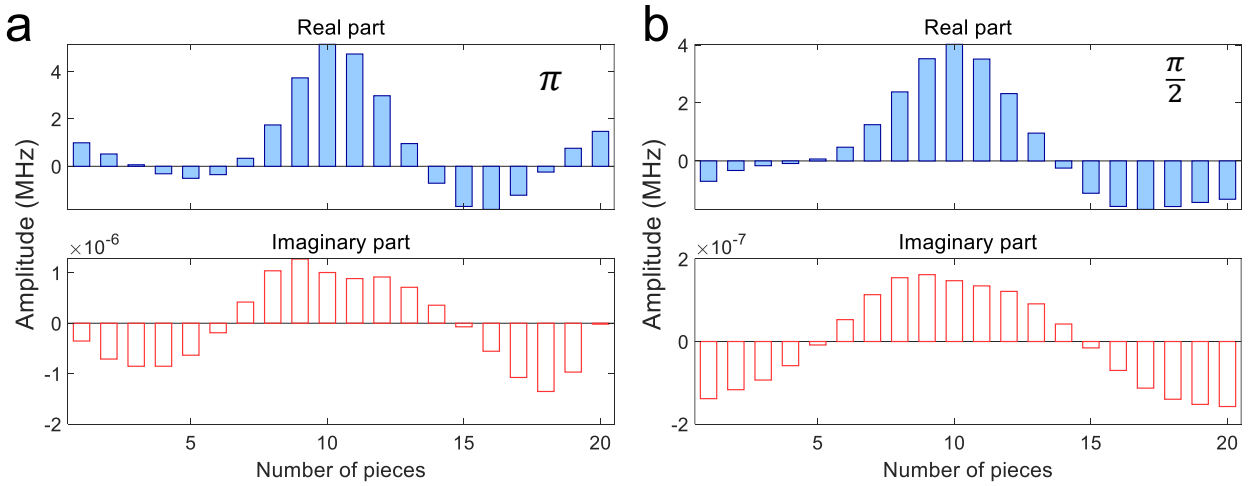

FIG. S7. **Optimal control for ^{14}N NV centers.** (a) The pulse sequence of the real (upper) and imaginary (lower) parts of the π pulses used in dynamical decoupling sequences and repetitive readout. The amplitude for each piece is denoted by Rabi frequency. Each piece lasts for 30 ns with 20 pieces in total. (b) The pulse sequence of the real (upper) and imaginary (lower) parts of the $\pi/2$ pulses. Each piece lasts for 30 ns with 20 pieces in total.

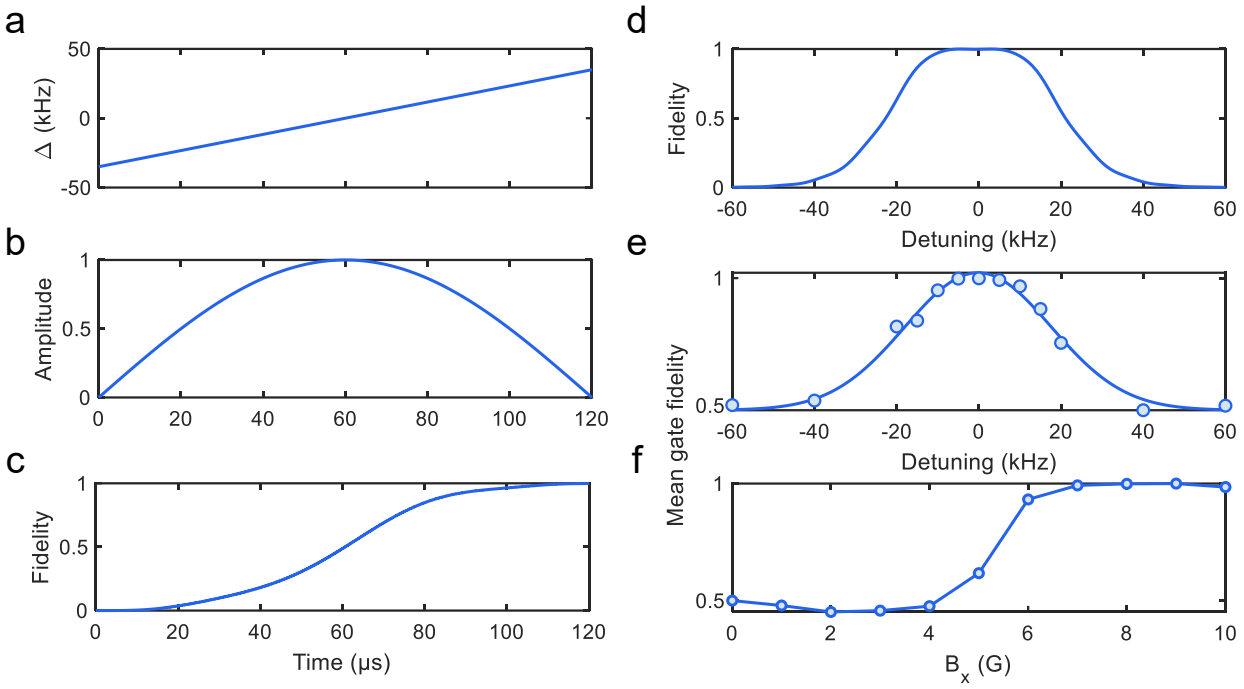

FIG. S8. **Adiabatic RF pulse design and robustness.** (a) Instantaneous detuning $\Delta(t)$ of the adiabatic pulse versus time, implementing a linear frequency sweep across the transition. (b) Corresponding amplitude envelope over the same duration. (c) Inversion fidelity versus time for a single adiabatic pulse at $B_x = 8$ G. (d) Inversion fidelity versus detuning at $B_x = 8$ G. (e) Mean gate fidelity for a train of 140 adiabatic π pulses versus detuning ($B_x = 8$ G). The train employs phase alternation, with each adjacent pair of pulses differing by π in phase. (f) Mean gate fidelity for 140 pulses versus drive amplitude B_x at zero detuning.

Single-cell NMR data summary		
№	Cell type	T_1 (ms)
1	HeLa	129(17)
2	HeLa	77(10)
3	HeLa	113(18)
4	HeLa	120(20)
5	HeLa	118(10)
6	HeLa	134(19)
7	HeLa	84(13)
8	HeLa	97(25)
9	MCF7	78(11)
10	MCF7	113(24)
11	MCF7	70(22)
12	MCF7	61(16)
13	MCF7	44(11)
14	MCF7	78(24)
15	MCF7	82(17)
16	MCF7	87(24)
17	MCF7	76(17)

FIG. S9. **Single-cell NMR T_1 data summary.** Multiple independent measurements were carried out for each cell type. NMR data were collected from 8 HeLa cells and 9 MCF7 cells. The right column reports the fitted T_1 values.